Meccanica
https://doi.org/10.1007/s11012-020-01218-x

B-bar virtual element method for nearly incompressible and compressible materials

Kyoungsoo Park · Heng Chi · Glaucio H. Paulino

Received: 5 February 2020 / Accepted: 22 July 2020

Abstract We present a B-bar formulation of the virtual element method (VEM) for the analysis of both nearly incompressible and compressible materials. The material stiffness is decomposed into dilatational and deviatoric parts, and only the deviatoric part of the material stiffness is utilized for stabilization of the element stiffness matrix. A feature of the formulation is that locking behavior for nearly incompressible materials is successfully removed by the spectral decomposition of the material stiffness. The eigenvalue analysis demonstrates that the method eliminates higher energy modes associated with locking behavior for nearly incompressible materials, while capturing constant strain energy modes for both compressible and nearly incompressible materials. The convergence and accuracy of the B-bar VEM are discussed using 2D and 3D examples with various element shapes (convex and non-convex).

K. Park (✉)
Department of Civil and Environmental Engineering, Yonsei University, 50 Yonsei-ro Seodaemun-gu, Seoul 03722, Korea
e-mail: k-park@yonsei.ac.kr

H. Chi
Siemens Corporate Technology, 755 College Rd E, Princeton, NJ 08540, USA

G. H. Paulino
School of Civil and Environmental Engineering, Georgia Institute of Technology, 790 Atlantic Drive, Atlanta, GA 30332, USA

Keywords B-bar method · Virtual element method · Nearly incompressible material · Eigenvalue analysis · Material stiffness splitting

1 Introduction

We present the B-bar formulation of the virtual element method (VEM) for the analysis of both nearly incompressible and compressible materials. Volumetric locking of nearly incompressible materials poses fundamental challenges in displacement-based methods, and thus various computational techniques have been developed to remove locking behavior [1–3]. Recently, the VEM has been proposed to handle general polygonal/polyhedral discretizations, and has been applied to various engineering problems [4–8]. In this work, the VEM is advanced further by establishing a general setting for a B-Bar formulation employing a diagonal matrix-based stabilization strategy, which has been shown to produce accurate results when compared to the traditional scalar-based stabilization strategy.

The remainder of the paper is organized as follows. Section 2 presents the VEM formulation and material stiffness splitting scheme for the analysis of both compressible and nearly incompressible materials. In Sect. 3, eigenvalue analysis is performed to investigate the effect of the stability term and associated

Published online: 10 August 2020

energy modes. In particular, the element stiffness matrices of the VEM (standard and B-Bar) are compared with those of the finite element method (FEM). Four computational examples are presented in Sect. 4. Finally, key findings of the present paper are summarized in Sect. 5.

2 B-bar VEM Formulation

Let us consider an elastic solid $\Omega \subset \mathbb{R}^d$ with $d \in \{2,3\}$ being the dimension number. On its boundary $\partial\Omega$, the solid is subjected to a traction field $\boldsymbol{t}$ on $\Gamma^{\boldsymbol{t}}$ and a prescribed displacement field $\boldsymbol{u}_0$ on $\Gamma^{\boldsymbol{u}}$, such that $\Gamma^{\boldsymbol{t}} \cap \Gamma^{\boldsymbol{u}} = \emptyset$ and $\Gamma^{\boldsymbol{t}} \cup \Gamma^{\boldsymbol{u}} = \partial\Omega$. With the boundary conditions, the equilibrating displacement field $\boldsymbol{u}$ is one among the set of kinematically admissible displacements $\mathcal{K}$ that satisfies

$$\int_{\Omega} \boldsymbol{\varepsilon}(\boldsymbol{v}) : (\mathbb{C}\boldsymbol{\varepsilon}(\boldsymbol{u}))\mathrm{d}\boldsymbol{x} = \int_{\Omega} \boldsymbol{f}\cdot\boldsymbol{v}\mathrm{d}\boldsymbol{x} + \int_{\Gamma^t} \boldsymbol{t}\cdot\boldsymbol{v}\mathrm{d}\boldsymbol{s} \quad \forall \boldsymbol{v} \in \mathcal{K}_0 \tag{1}$$

where $\mathbb{C}$ is the fourth order elastic modulus tensor, $\boldsymbol{v}$ is an arbitrary virtual displacement, $\mathcal{K}_0$ stands for the set of admissible displacements which vanishes on $\Gamma^{\boldsymbol{u}}$, $\boldsymbol{\varepsilon}(\cdot) = 1/2\left[\nabla(\cdot) + \nabla(\cdot)^T\right]$ is the linearized strain operator, and $\boldsymbol{f}$ is a prescribed body force.

In this work, we introduce a B-bar VEM approximation to the above continuous variational principle for linear elasticity problems, which is free of volumetric locking. Let us consider a discretization Ω_h of the solid into non-overlapping elements. We further assume that the discretization is subjected to applied tractions and displacements on $\Gamma^{\boldsymbol{t}}_h$ and $\Gamma^{\boldsymbol{u}}_h$ such that $\Gamma^{\boldsymbol{t}}_h \cap \Gamma^{\boldsymbol{u}}_h = \emptyset$ and $\Gamma^{\boldsymbol{t}}_h \cup \Gamma^{\boldsymbol{u}}_h = \partial\Omega_h$, and that $\Gamma^{\boldsymbol{t}}_h$ and $\Gamma^{\boldsymbol{u}}_h$ are compatible with $\Gamma^{\boldsymbol{t}}$ and $\Gamma^{\boldsymbol{u}}$. We denote E as a generic element in Ω_h. With the introduction, the global virtual element space $\mathcal{K}_h$ for the displacement field ($\mathbf{v}_h$) is defined as

$$\mathcal{K}_h = \left\{ \mathbf{v}_h \in \mathcal{K} : \mathbf{v}_h|_E \in [\mathcal{V}(E)]^d, \forall E \in \Omega_h \right\} \tag{2}$$

where $\mathcal{V}(E)$ is the local virtual element space, which will be defined in the following subsections. In this work, the construction of local virtual element spaces $\mathcal{V}(E)$ follows the procedures introduced in references [9, 10]. The discussion will focus on linear virtual elements and we remark that the proposed B-Bar VEM formulation can be readily extended to higher-order virtual elements as well.

2.1 Virtual element space in 2D

In the 2D case, a generic E is assumed to be a polygon made up of straight edges. Let us denote e as a generic edge of E. We first define an auxiliary space $\tilde{\mathcal{V}}(E)$ as

$$\tilde{\mathcal{V}}(E) = \left\{ v \in \mathcal{H}_1(E) : \Delta v \in \mathcal{P}_1(E) \text{ and } v|_e \in \mathcal{P}_1(e) \forall e \in \partial E \right\} | \tag{3}$$

where $\mathcal{P}_1(\cdot)$ is the space of linear functions and Δ stands for the Laplacian operator. Notice that the above definition implies $\mathcal{P}_1(E) \subset \tilde{\mathcal{V}}(E)$ and, thus, we can define a projection operator $\Pi^{\nabla}_E : \tilde{\mathcal{V}}(E) \to \mathcal{P}_1(E)$ such that, for any given $v \in \tilde{\mathcal{V}}(E)$, we have

$$\int_E \nabla\left(\Pi^{\nabla}_E v\right) \cdot \nabla p \mathrm{d}\boldsymbol{x} = \int_E \nabla v \cdot \nabla p \mathrm{d}\boldsymbol{x} \quad \forall p \in \mathcal{P}_1(E) \tag{4}$$

and

$$\int_{\boldsymbol{x}_v \in E} (\Pi^{\nabla}_E v)(\boldsymbol{x}_v) = \int_{\boldsymbol{x}_v \in E} v(\boldsymbol{x}_v), \tag{5}$$

where $\boldsymbol{x}_v$ is a generic vertex of E. Applying integration by parts and simplifying Eq. (4), we obtain

$$\int_E \nabla\left(\Pi^{\nabla}_E v\right)\mathrm{d}\boldsymbol{x} = \int_{\partial E} v\boldsymbol{n}\mathrm{d}s, \tag{6}$$

where $\boldsymbol{n}$ is the unit outward normal vector on ∂E.

Equations (5) and (6) suggest that the projection $\Pi^{\nabla}_E v$ can be computed using only the values of v on the vertices of E. After defining the auxiliary space $\tilde{\mathcal{V}}(E)$ and projection operator Π^{∇}_E, the local virtual element space $\mathcal{V}(E)$ is defined as

$$\mathcal{V}(E) = \left\{ v \in \tilde{\mathcal{V}}(E) : \int_E \left(\Pi^{\nabla}_E v - v\right) p \mathrm{d}\boldsymbol{x} = 0 \forall p \in \mathcal{P}_1(E) \right\}. \tag{7}$$

2.2 Virtual element space in 3D

In the 3D case, a generic element E is assumed to be a polyhedron consisting of planar faces. Let us denote F as a generic face of E. Similarly to the 2D case, we first define an auxiliary space $\tilde{\mathcal{V}}(E)$ as

$$\tilde{\mathcal{V}}(E) = \{v \in \mathcal{H}_1(E) : \Delta v \in \mathcal{P}_1(E) \quad \text{and } v|_F \in \mathcal{V}(F) \forall F \in \partial E\} \tag{8}$$

where $\mathcal{V}(F)$ is the local space on face F, which is equivalent to the local virtual element space in 2D [Eq. (7)]. Since we have $\mathcal{P}_1(E) \subset \tilde{\mathcal{V}}(E)$, we define the projection operator $\Pi_E^\nabla : \tilde{\mathcal{V}}(E) \to \mathcal{P}_1(E)$ according to conditions of Eqs. (4)–(6). In particular, we expand Eq. (6) as

$$\int_E \nabla(\Pi_E^\nabla v) \mathrm{d}\boldsymbol{x} = \int_{\partial E} v \boldsymbol{n} \mathrm{d}s = \sum_{F \in \partial E} \left(\int_F v \mathrm{d}s \right) \boldsymbol{n}_F \tag{9}$$

where $\boldsymbol{n}_F$ is the (constant) outward normal vector of face F (which is a constant vector over F). According to the definition of $\mathcal{V}(F)$ [Eq. (7)], $\int_F v \mathrm{d}s$ can be computed through $\int_F \Pi_E^\nabla v \mathrm{d}s$ using the values of v on the vertices of face F. As a result, the projection $\Pi_E^\nabla v$ can be computed using only the values of v on the vertices of E. By means of $\tilde{\mathcal{V}}(E)$ and the projection operator Π_E^∇, the formal definition of the local virtual element space $\mathcal{V}(E)$ in 3D can be obtained using Eq. (7) as in the 2D case.

2.3 L^2 Projection operators

The local virtual element space $\mathcal{V}(E)$ contains functions, which are only known implicitly in the interior of E. In order to construct a VEM approximation, we define an L^2 projection operator $\Pi^0 : \mathcal{V}(E) \to \mathcal{P}_1(E)$ such that for any given $v \in \mathcal{V}(E)$, we have

$$\int_E \Pi^0 v p \mathrm{d}\boldsymbol{x} = \int_E v p \mathrm{d}\boldsymbol{x} \quad \forall p \in \mathcal{P}_1(E) \tag{10}$$

According to the definition of the local space $\mathcal{V}(E)$, we can show that $\Pi^0 v = \Pi_E^\nabla v$. As a result (same as $\Pi_E^\nabla v$), this L^2 projection ($\Pi^0 v$) can be computed exactly using only the values of v on the vertices of E. We refer to reference [11] for the computational implementation of the L^2 projection operator. The above discussion focus on the L^2 projection of scalar functions $v \in \mathcal{V}(E)$. For vector-valued functions $\boldsymbol{v} \in [\mathcal{V}(E)]^d$, we will use $\boldsymbol{\Pi}^0 \boldsymbol{v}$ to denote its L^2 projection, such that $\boldsymbol{\Pi}^0 \boldsymbol{v} = \left[\Pi^0 v_x, \Pi^0 v_y\right]^T$ for $d = 2$ and $\boldsymbol{\Pi}^0 \boldsymbol{v} = \left[\Pi^0 v_x, \Pi^0 v_y, \Pi^0 v_z\right]^T$ for $d = 3$.

2.4 B-bar VEM approximation through material stiffness splitting

For nearly incompressible linear elastic solids, volumetric locking typically occurs in FEM and VEM solutions. To address this issue in VEM, we propose a general B-bar formulation, which is free of volumetric locking over a wide spectrum of Poisson's ratio.

The basic idea of the proposed B-bar VEM is based on a deviatoric-dilatational splitting of the elasticity modulus tensor [12]. Using the common matrix representation of the modulus tensor, the elasticity modulus matrix, denoted by $\boldsymbol{C}$, can be expressed in the spectral form as

$$\boldsymbol{C} = \sum_{i=1}^{d(d+1)/2} \lambda_i \boldsymbol{m}_i \boldsymbol{m}_i^T \tag{11}$$

where λ_i is the ith eigenvalue of matrix $\boldsymbol{C}$ and $\boldsymbol{m}_i$ is the associated eigenvector such that $\boldsymbol{m}_i^T \boldsymbol{m}_i = 1$. In the sequel, we will focus on the 3D case. For isotropic linear elastic materials, we can show that $\boldsymbol{m}_1 = \frac{1}{\sqrt{3}}[1,1,1,0,0,0]^T$ is an eigenvector of the matrix $\boldsymbol{C}$, and the corresponding eigenvalue is the bulk modulus, namely, $\lambda_1 = 3\kappa$. Based on this observation, we decompose the elastic modulus matrix $\boldsymbol{C}$ as

$$\boldsymbol{C} = \boldsymbol{C}_{dev} + \boldsymbol{C}_{dil}, \tag{12}$$

where

$$\boldsymbol{C}_{dil} = \lambda_1 \boldsymbol{m}_1 \boldsymbol{m}_1^T \quad \text{and} \quad \boldsymbol{C}_{dev} = \boldsymbol{C} - \lambda_1 \boldsymbol{m}_1 \boldsymbol{m}_1^T. \tag{13}$$

We remark that, although the above deviatoric and dilatational splitting is presented for the 3D case, the same idea and formalism are also applicable to the 2D case under plane strain conditions. For the 2D case, the eigenvector $\boldsymbol{m}_1$ is $\frac{1}{\sqrt{2}}[1,1,0]^T$ and the corresponding eigenvalue is associated with the bulk modulus, i.e., $\lambda_1 = 2\kappa + \frac{2\mu}{3}$, where μ is the shear modulus. We also remark that, in this work, instead of splitting the $\boldsymbol{B}$ matrix as in the classical B-bar methods [13], we propose to split the elasticity modulus matrix $\boldsymbol{C}$. *In Appendix B, we will show that these two approaches are in fact equivalent.*

Having introduced the decomposition of $\boldsymbol{C}$ into deviatoric and dilatational components, we are now ready to introduce the B-bar VEM approximation of linear elasticity problems. The key step is how we

construct the element-level stiffness matrix $\boldsymbol{K}_E = \boldsymbol{K}_E^C + \boldsymbol{K}_E^S$, which consists of a consistency part and a stability part. In addition, based on the material stiffness splitting [Eqs. (12)–(13)], the proposed B-bar VEM formulation further decomposes the consistency part of the stiffness matrix $\boldsymbol{K}_E^C$ as

$$\begin{aligned}\boldsymbol{K}_E^C &= \boldsymbol{K}_{E,dev}^C + \boldsymbol{K}_{E,dil}^C \\ &= \int_E \boldsymbol{B}_c^T \boldsymbol{C}_{dev} \boldsymbol{B}_c d\boldsymbol{x} + \int_E \boldsymbol{B}_c^T \boldsymbol{C}_{dil} \boldsymbol{B}_c d\boldsymbol{x}\end{aligned} \tag{14}$$

The matrix $\boldsymbol{B}_c$ reads as

$$\boldsymbol{B}_c = \begin{bmatrix} \boldsymbol{b}\left(\Pi^0 \phi_1\right) & \dots & \boldsymbol{b}\left(\Pi^0 \phi_n\right) \end{bmatrix} \tag{15}$$

where we recall that $\Pi^0 \phi_i$ is the L^2 projection of the ith local basis function ϕ_i of the local space $\mathcal{V}(E)$; n is the total number of nodes in E; and matrix $\boldsymbol{b}\left(\Pi^0 \phi_i\right)$ is given by

$$\boldsymbol{b}\left(\Pi^0 \phi_i\right) = \begin{bmatrix} \dfrac{\partial \Pi^0 \phi_i}{\partial x} & 0 \\ 0 & \dfrac{\partial \Pi^0 \phi_i}{\partial y} \\ \dfrac{\partial \Pi^0 \phi_i}{\partial y} & \dfrac{\partial \Pi^0 \phi_i}{\partial x} \end{bmatrix} \quad \text{in 2D} \tag{16}$$

and

$$\boldsymbol{b}\left(\Pi^0 \phi_i\right) = \begin{bmatrix} \dfrac{\partial \Pi^0 \phi_i}{\partial x} & 0 & 0 \\ 0 & \dfrac{\partial \Pi^0 \phi_i}{\partial y} & 0 \\ 0 & 0 & \dfrac{\partial \Pi^0 \phi_i}{\partial z} \\ \dfrac{\partial \Pi^0 \phi_i}{\partial y} & \dfrac{\partial \Pi^0 \phi_i}{\partial x} & 0 \\ 0 & \dfrac{\partial \Pi^0 \phi_i}{\partial z} & \dfrac{\partial \Pi^0 \phi_i}{\partial y} \\ \dfrac{\partial \Pi^0 \phi_i}{\partial z} & 0 & \dfrac{\partial \Pi^0 \phi_i}{\partial x} \end{bmatrix} \quad \text{in 3D} \tag{17}$$

Notice that, the matrix $\boldsymbol{B}_c$ is a function of the L^2 projection of the basis function, which can be computed using only the geometric information of E.

For linear virtual elements, $\boldsymbol{B}_c$ is a constant matrix and the final expressions for $\boldsymbol{K}_{E,dev}^C$, $\boldsymbol{K}_{E,dil}^C$, and $\boldsymbol{K}_E^C$ are given by

$$\boldsymbol{K}_{E,dev}^C = |E| \boldsymbol{B}_c^T \boldsymbol{C}_{dev} \boldsymbol{B}_c \tag{18}$$

$$\boldsymbol{K}_{E,dil}^C = |E| \boldsymbol{B}_c^T \boldsymbol{C}_{dil} \boldsymbol{B}_c \tag{19}$$

and

$$\boldsymbol{K}_E^C = |E| \boldsymbol{B}_c^T \boldsymbol{C}_{dev} \boldsymbol{B}_c + |E| \boldsymbol{B}_c^T \boldsymbol{C}_{dil} \boldsymbol{B}_c = |E| \boldsymbol{B}_c^T \boldsymbol{C} \boldsymbol{B}_c \tag{20}$$

We remark that, in the proposed B-bar VEM formulation, the final expression of the consistency part of the local stiffness matrix is the same as the one in the standard VEM formulation. In fact, this remark also holds true to higher-order cases.

On the other hand, the stability part of the stiffness matrix $\boldsymbol{K}_E^S$ in the B-bar VEM formulation is given by the popular diagonal-based recipe [8, 14–16] as

$$\boldsymbol{K}_E^S = \left(\boldsymbol{I} - \boldsymbol{P}^0\right)^T \boldsymbol{\Lambda}_{E,dev} \left(\boldsymbol{I} - \boldsymbol{P}^0\right) \tag{21}$$

where $\boldsymbol{P}^0$ is the matrix representation of the L^2 projection operator $\boldsymbol{\Pi}^0$ [6, 11], and $\boldsymbol{\Lambda}_{E,dev}$ is a diagonal matrix of the form

$$\boldsymbol{\Lambda}_{E,dev} = \max\left(\left[\boldsymbol{K}_{E,dev}^C \right]_{ii}, \mu/2 \right) \tag{22}$$

We highlight that the stability part of the stiffness matrix $\boldsymbol{K}_E^S$ in the B-bar VEM formulation is different from the ones in the standard VEM for linear elasticity. In fact, $\boldsymbol{K}_E^S$ in the proposed B-bar VEM formulation depends only on the deviatoric component of the stiffness matrix $\boldsymbol{K}_{E,dev}^C$. As we will demonstrate in Sect. 3, by defining the stability part of the stiffness matrix in such manner, we can successfully eliminate the artificial overstiff deformation eigen-modes from the element-level VEM stiffness matrix. As for the approximation of the loading term, the proposed B-bar VEM formulation follows the same construction as the standard VEM formulation [17, 18].

Before we conclude this section, we highlight that, compared to the B-bar VEM formulation introduced in [16], the present B-bar VEM formulation has the following advantages. First, the present B-bar VEM formulation introduces a diagonal matrix-based stabilization strategy, which is typically more accurate than the traditional scalar-based stabilization strategy. Second, the present B-bar framework enjoys a more general setting. For example, it can be applied to

higher-order virtual elements and the idea of splitting the elasticity modulus based on spectral decomposition can be extended to construct locking-free VEM formulation for anisotropic elastic solids, e.g., fiber-reinforced composites [12, 19, 20]. Alternatively, the stability term may be computed by modifying the Lame parameters in relation with element shape [21], but one needs to introduce a subtriangular mesh for each element.

3 Eigenvalue analysis

The element stiffness matrices of VEM are compared with those of FEM to investigate the effect of the stability term by means of eigenvalue analyses. Polygonal and polyhedral meshes are generated within unit square and cube domains, as shown in Fig. 1a and b, respectively. The number of elements is 50 for each mesh. The elastic modulus is arbitrarily selected as 100, and two cases of Poisson's ratio are employed, i.e., 0.25 (compressible material case) and 0.49995 (nearly incompressible material case). Eigenvalues of each element stiffness matrix ($\boldsymbol{K}_E$) are computed using three approaches, i.e., (1) FEM, (2) standard VEM, and (3) B-bar VEM. For the construction of FEM element stiffness matrices, the Wachspress shape functions [22] are employed. For the case of compressible materials, Fig. 2 demonstrates that eigenvalues of each element, obtained from the three approaches, are within the same order of magnitude for both 2D and 3D cases. For the case of nearly incompressible materials ($\nu = 0.49995$), the eigenvalues of each element are shown in Fig. 3. While those eigenvalues are widely distributed for the standard

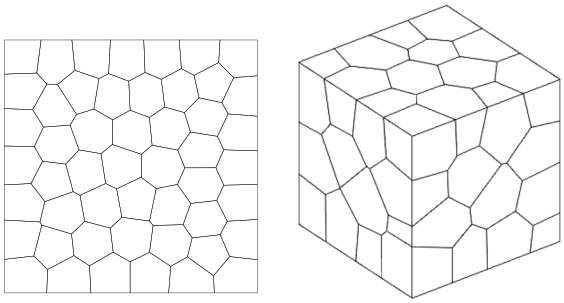

Fig. 1 **a** Polygonal and **b** polyhedral meshes for eigenvalue analysis

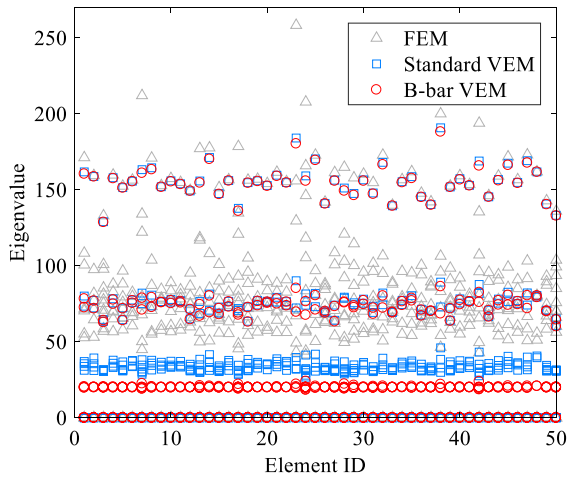

(a)

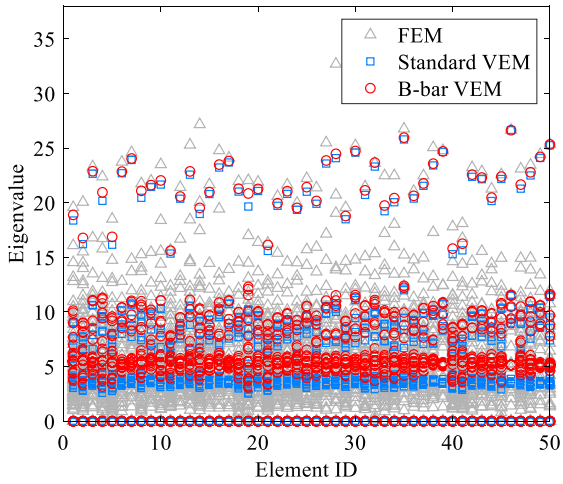

(b)

Fig. 2 Eigenvalues of element stiffness matrices for compressible material: **a** polygonal mesh (2D), and **b** polyhedral mesh (3D)

FEM, they are clustered within certain ranges for both the standard VEM and the B-bar VEM. One should note that the maximum eigenvalue is several orders of magnitude larger than the other eigenvalues for the B-bar VEM, and the maximum eigenvalue of each element is associated with the dilation mode.

To confirm associated energy modes in VEM, the element stiffness matrix ($\boldsymbol{K}_E$) is split into two parts, i.e., consistency and stability terms. For FEM, we note that $\boldsymbol{K}_E^C$ and $\boldsymbol{K}_E^S$ are computed using the projection operator (Π_E^{∇}), which isolates higher order modes in

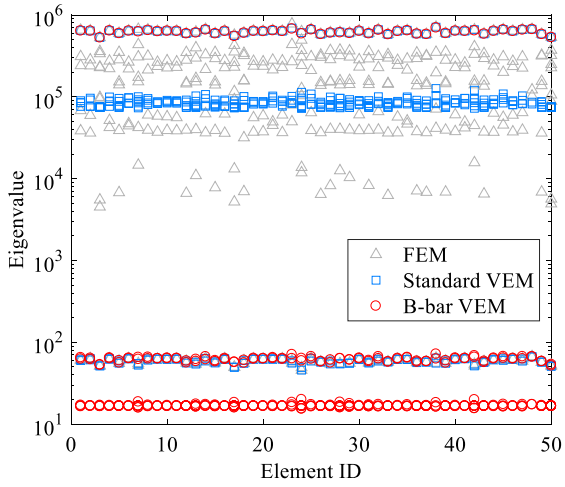

(a)

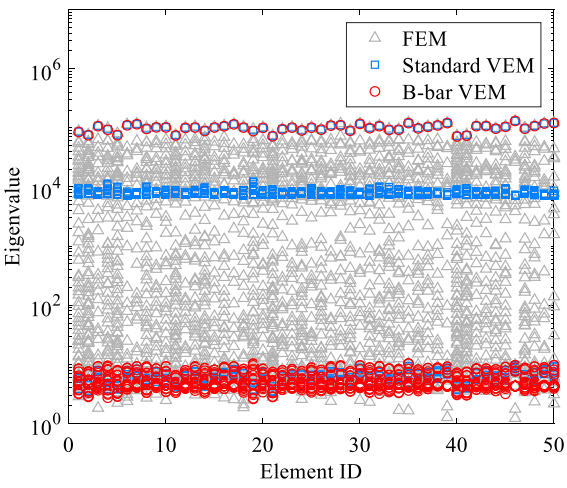

(b)

Fig. 3 Eigenvalues of element stiffness matrices for nearly incompressible materials: **a** polygonal mesh (2D), and **b** polyhedral mesh (3D)

the eigenvalue analysis. Then, $\boldsymbol{K}_E^S$ and $\boldsymbol{K}_E^C$ of FEM are given as

$$\boldsymbol{K}_E^S = \left(\boldsymbol{I} - \boldsymbol{P}^0\right)^T \boldsymbol{K}_{E,FEM} \left(\boldsymbol{I} - \boldsymbol{P}^0\right) \tag{23}$$

and

$$\boldsymbol{K}_E^C = \mathbf{K}_{E,FEM} - \boldsymbol{K}_E^S \tag{24}$$

respectively, where $\boldsymbol{K}_{E,FEM}$ is the element stiffness matrix obtained from FEM.

For the polyhedral mesh (Fig. 1b) with the Poisson's ratio of 0.49995, the eigenvalues of $\boldsymbol{K}_E^C$ and $\boldsymbol{K}_E^S$ are calculated according to FEM, standard VEM, and B-bar VEM (see Fig. 4). For each case, Fig. 4a displays six non-zero eigenvalues of $\boldsymbol{K}_E^C$, which correspond to constant strain energy modes, while the other eigenvalues of $\boldsymbol{K}_E^C$ are zero. The maximum eigenvalue of each element, associated with the dilation mode, is several orders of magnitude larger than the other eigenvalues for the nearly incompressible material, as expected. Furthermore, FEM and VEM display almost identical eigenvalues for the constant strain energy modes. For higher order modes,

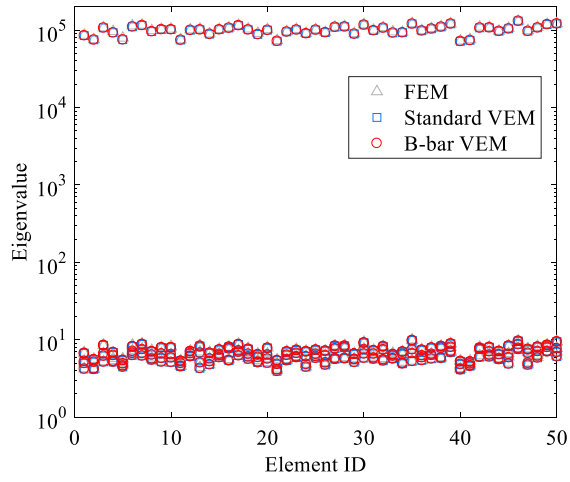

(a)

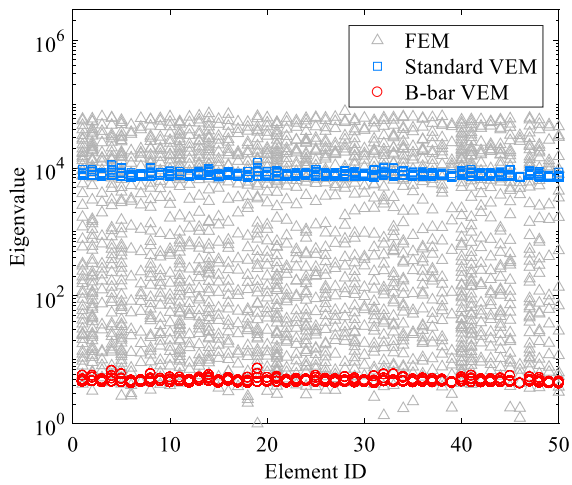

(b)

Fig. 4 Eigenvalues of **a** consistency term ($\boldsymbol{K}_{E,C}$) and **b** stability term ($\boldsymbol{K}_{E,S}$) for the polyhedral mesh

the computed eigenvalues are widely distributed for FEM, while they are clustered in a certain range for standard VEM and B-bar VEM, as shown in Fig. 4b. Furthermore, for the case of B-bar VEM, the eigenvalues of higher energy modes are in the range of the eigenvalues of constant strain energy modes without dilation. Thus, B-bar VEM can remove locking behavior for nearly incompressible materials, as illustrated with examples in the following section.

4 Computational examples

Four computational examples are employed to verify the VEM with the B-bar method for both nearly incompressible and compressible materials. The convergence of displacement solutions is investigated with various element shapes, i.e., convex and non-convex, for both two- and three-dimensional problems.

4.1 Cantilever

A cantilever has a rectangular domain with the length (L) of 2 and the depth (D) of 1, as shown in Fig. 5 (consistent units). The elastic modulus (E) is assumed as 10^5. The Poisson's ratio is selected as 0.25 and 0.49995, which correspond to compressible and nearly incompressible materials, respectively. Plane strain is assumed with unit thickness. The traction boundary condition is imposed on the right edge considering a quadratic function, i.e., $P_y(y) = 6P_0(0.25 - y^2)$, where P_0 is -100 and the resultant force (P) of the traction (P_y) is -100. The prescribed displacement boundary conditions are applied on the left edge, which are obtained from the analytical solution [23] for the horizontal and vertical displacements:

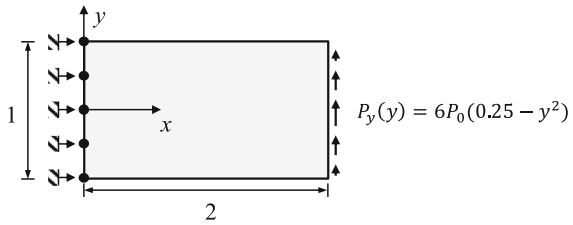

Fig. 5 Geometry and boundary conditions of the cantilever example

$$u_x = -\frac{Py}{6\bar{E}I}\left((6L - 3x)x + (2 + \bar{\nu})y^2 - \frac{3D^2}{2}(1 + \bar{\nu})\right) \tag{25}$$

and

$$u_y = \frac{P}{6\bar{E}I}\left(3\bar{\nu}y^2(L - x) + (3L - x)x^2\right) \tag{26}$$

respectively, where $\bar{E} = E/(1 - \nu^2)$ and $\bar{\nu} = \nu/(1 - \nu)$ for the plane strain condition. Then, the domain is discretized into three types of polygonal meshes, i.e., centroidal Voronoi tessellation (CVT), Pegasus, and "VEM", as illustrated in Fig. 6. For each

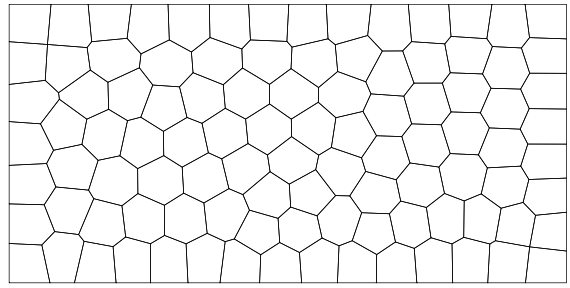

(a)

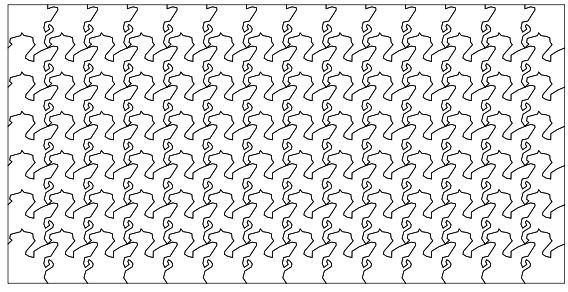

(b)

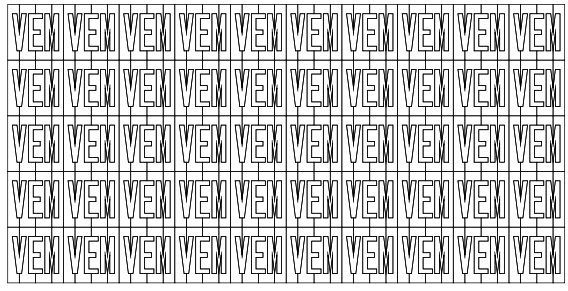

(c)

Fig. 6 Polygonal meshes for the cantilever example: **a** CVT mesh, **b** Pegasus mesh, and **c** "VEM" mesh

mesh type, seven virtual element meshes are generated to investigate the rate of convergence for the B-bar VEM.

For each element type, L^2 type error of displacement is evaluated according to element size. The element size is estimated by the square root of the average area of elements in the polygonal meshes. Figure 7a and b demonstrate that the optimal rate of convergence is achieved for both compressible and nearly incompressible materials, respectively, regardless of element shapes, i.e., convex and non-convex. Because of element quality, CVT meshes (Fig. 7a) provides more accurate results than Pegasus and "VEM" meshes (Fig. 7b and c), as expected.

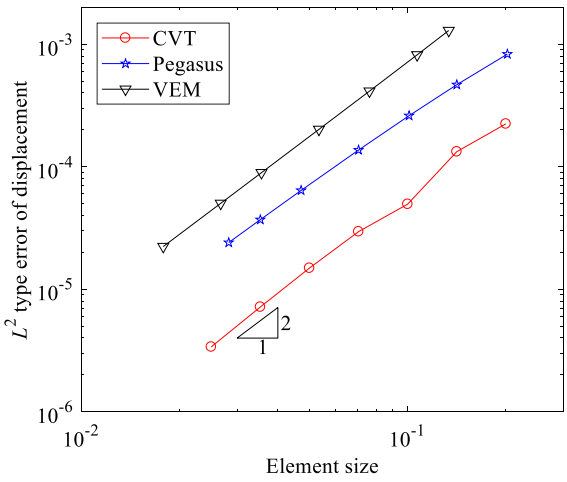

(a)

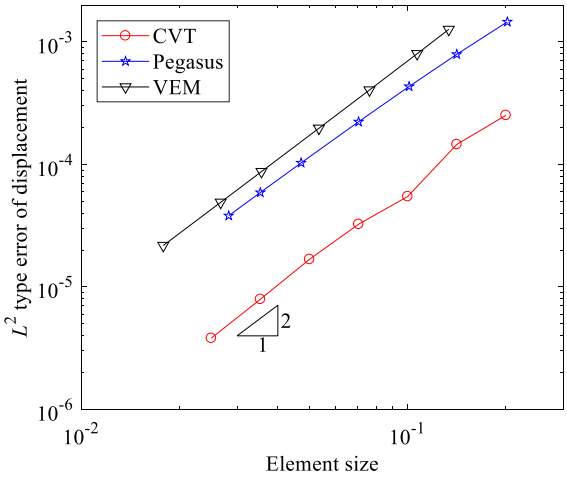

(b)

Fig. 7 Rate of convergence for L^2 type error of displacement for **a** compressible material (ν = 0.25), and **b** nearly incompressible material (ν = 0.49995). Each point on the plots refers to a single mesh

4.2 Flat punch

The flat punch problem consists of a square domain of dimensions by 1 by 1, in which the uniform vertical displacement of -0.03 is applied on the one-third portion of the top edge, while the left, right, and bottom edges are constrained along the surface normal direction, as shown in Fig. 8 (consistent units). The elastic modulus is 250, and the Poisson ratio is 0.49995. When the domain is discretized into CVT meshes, the edges of polygonal elements do not exactly match with the displacement boundary of the top edge, i.e., $1/3 \leq x \leq 2/3$. To fit with the region of the displacement boundary condition, two approaches are employed, i.e., node relocation and edge split, as shown in Fig. 9a and b, respectively. Nodes are relocated to the position x = 1/3 and x = 2/3, which correspond to solid red circles in Fig. 9a. For the other approach, edges are split, and new nodes are created at x = 1/3 and x = 2/3, as shown by solid red circles in Fig. 9b. Alternatively, the combination of the edge split and node relocation may improve mesh quality according to the ratio of the split edge length to the original edge length [24].

The flat punch problem is solved using the B-bar VEM. The number of polygonal elements is 100, 800, and 6400. Figures 10a and b show the vertical displacement of the top edge using the CVT meshes obtained from the node relocation and edge split approaches, respectively. Both approaches

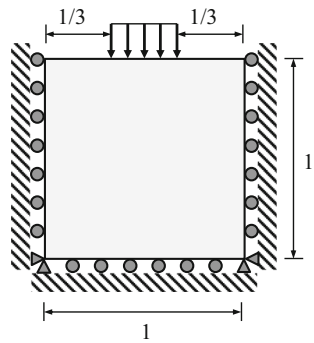

Fig. 8 Geometry and boundary conditions of the flat punch example

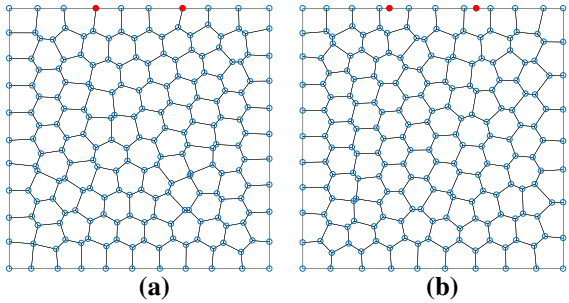

Fig. 9 Two types of CVT meshes using **a** nodal relocation, and **b** edge split to match with the displacement boundary condition

demonstrate the convergence of the vertical displacement under mesh refinement. The Abaqus [25] solution in Fig. 10 is obtained from a FE mesh consisting of 900 × 900 bilinear quadrilateral elements with constant pressure, which leads to 810,000 elements. Additionally, the problem is solved using the standard VEM, which yields the vertical displacement relatively away from the Abaqus solution, as shown in Fig. 11. The pressure field is also computed using the B-bar VEM and standard VEM, as shown in Fig. 12a and b, respectively. The B-bar VEM provides the smooth pressure field, while the standard VEM cannot represent the smooth pressure field for nearly incompressible material.

4.3 Cook's beam benchmark

Cook's beam example is employed for both compressible and nearly incompressible materials. The elastic modulus is 250, and the previous two cases of Poisson's ratio are employed, i.e., 0.25 and 0.49995, with the plane strain condition. The geometry and boundary conditions are shown in Fig. 13 (consistent units). The beam is discretized using CVT, random Voronoi tessellation (RVT), Pegasus and bird meshes. For the CVT and RVT meshes (e.g., Figures 14a and b), the number of elements is 25, 50, 100, 200, and 400. For the Pegasus and bird meshes, 5 × 5, 7 × 7, 10 × 10, 15 × 15, and 20 × 20 grids are first generated within a unit square, and nodal coordinates are linearly transformed to fit within the given geometry. The Pegasus and bird meshes with 5 × 5 grid are illustrated in Fig. 14c and d, respectively. Then, the vertical displacement is evaluated at the upper-right corner of the domain.

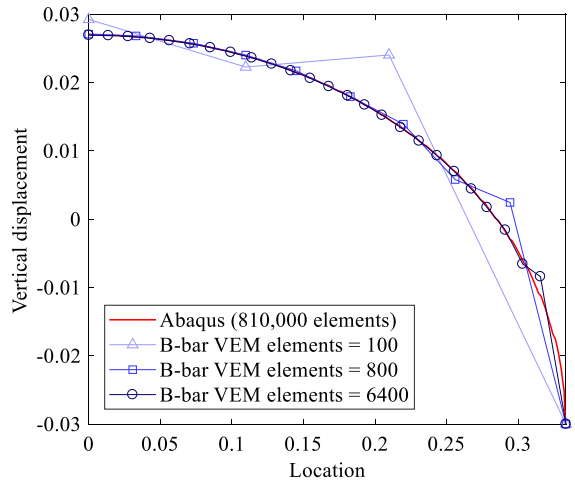

Fig. 10 B-bar VEM study for convergence of the vertical displacement on surface: **a** node relocation approach, and **b** edge split approach

Figures 15a and b demonstrate the convergence of the vertical displacement to the Abaqus solution for both compressible and nearly incompressible materials, respectively. For the Abaqus solution, the domain is discretized using 1,000,000 bilinear quadrilateral elements with constant pressure. The Abaqus vertical displacement at the tip of the beam is 9.444 and 7.769 for the Poisson's ratio of 0.25 and 0.49995, respectively.

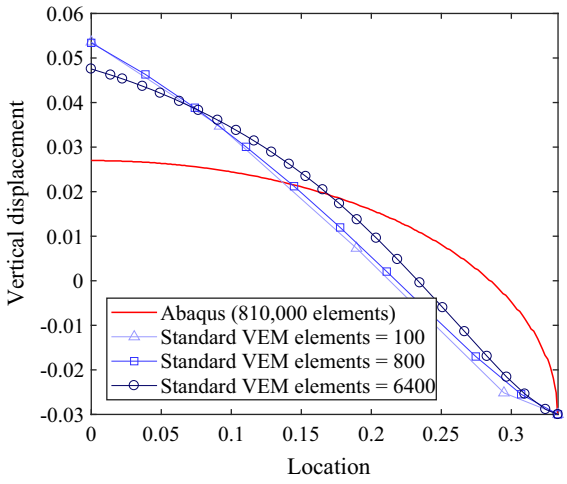

Fig. 11 Standard VEM study for convergence of the vertical displacement on surface. Comparison with the results of Fig. 10 shows the superiority of the B-bar VEM

Figure 16 illustrates the case of $\nu = 0.49995$, and compares the computational results of B-bar VEM with B-bar FEM, standard VEM, and standard FEM. The B-bar method improves the computational results for both VEM and FEM, as expected. Furthermore, the B-bar VEM provides far more accurate results than the B-bar FEM. However, monotonic convergence is not guaranteed for the B-bar VEM when the number of elements is relatively small. Additionally, the pressure fields of the Pegasus and bird meshes are plotted in Fig. 17a and b, respectively, for the Poisson's ratio of 0.49995. Although highly non-convex elements are employed, the smooth pressure fields are achieved for nearly incompressible material.

We investigate the effect of Poisson's ratio on the displacement solution. The Poisson's ratio is selected as 0.0, 0.3, 0.4, 0.49, and 0.49995, and the CVT mesh is used with 400 elements. The four computational approaches are employed, i.e., VEM with B-bar method, FEM with B-bar method, standard VEM, and standard FEM. When the Poisson's ratio is smaller than 0.4, the computational results are similar among the approaches, as shown in Fig. 18. For the case of nearly incompressible material ($\nu = 0.49995$), the B-bar VEM provides the most accurate result among the four approaches, as discussed previously.

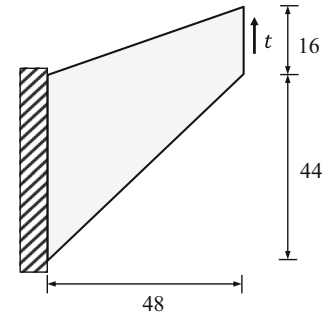

Fig. 13 Geometry and boundary conditions of the Cook's beam problem

4.4 Compression of 3D constrained block

For 3D analysis, a constrained block of $1 \times 0.5 \times 0.5$ is employed, as shown in Fig. 19 (consistent units). The uniform displacement of -0.05 is applied on the half top surface along the vertical direction, and the traction-free boundary condition is imposed on the other half top surface. On the front, back, left, right, and bottom surfaces, displacements are constrained along the surface normal directions. The box domain is initially discretized into polyhedral elements using

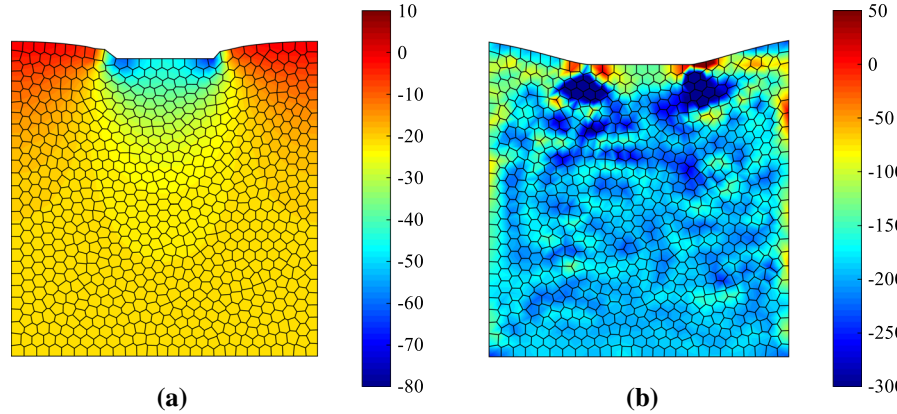

Fig. 12 Computational result of the pressure field using **a** VEM with the B-bar method, and **b** standard VEM

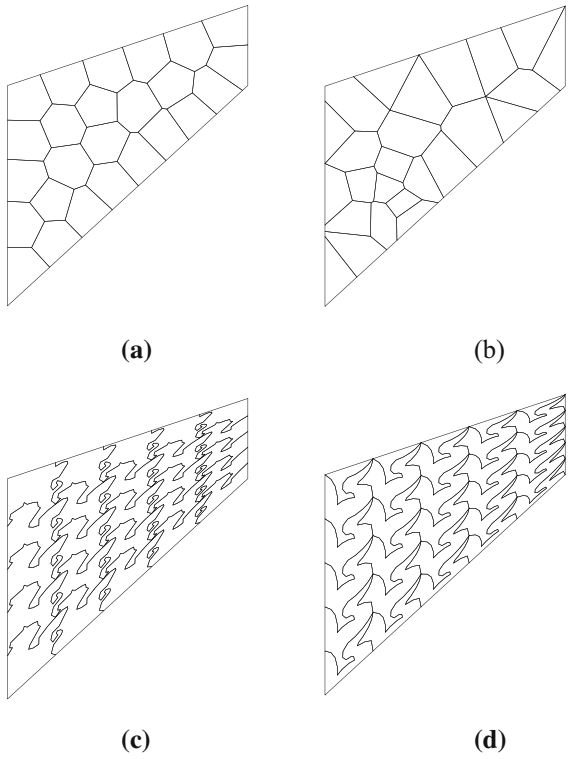

Fig. 14 VEM meshes for the Cook's beam problem: **a** CVT mesh, **b** RVT mesh, **c** Pegasus mesh, and **d** Bird mesh

CVT elements (Fig. 20a). To match faces of polyhedral elements with the area of the displacement boundary of the top surface, we simply split faces, which leads to new nodes and edges (Fig. 20b). The elastic modulus and Poisson's ratio are assumed as 1000 and 0.49995, respectively.

The convergence of displacement solution is investigated by mesh refinement. The number of polyhedral elements is 500, 1000, 2000, 4000, 8000, and 16000. The averaged vertical displacement along the upper-left edge of the block is plotted according to the number of elements (Fig. 21). The B-bar VEM provides far more accurate solution than the standard VEM. The Abaqus [25] solution is obtained using 2,000,000 8-node linear brick elements with constant pressure. The Abaqus vertical displacement is 0.07302. Additionally, the contour of the displacement and pressure fields is plotted in Figs. 22 and 23, respectively. Both B-bar VEM and standard VEM

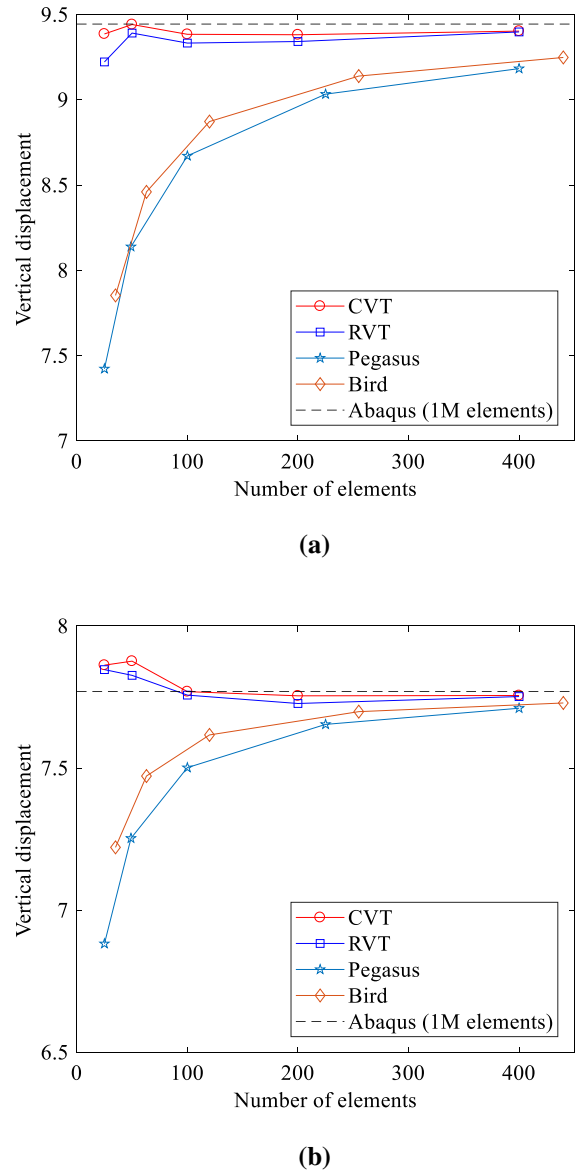

Fig. 15 Convergence of vertical displacement for Cook's beam problem: **a** compressible material ($\nu = 0.25$), and **b** nearly incompressible material ($\nu = 0.49995$). Each point on the plots refers to a single mesh

provide smooth displacement fields although the standard VEM has relatively large error. However, the B-bar VEM accurately captures the smooth pressure filed (Fig. 23a), while the standard VEM results in inaccurate pressure field (Fig. 23b).

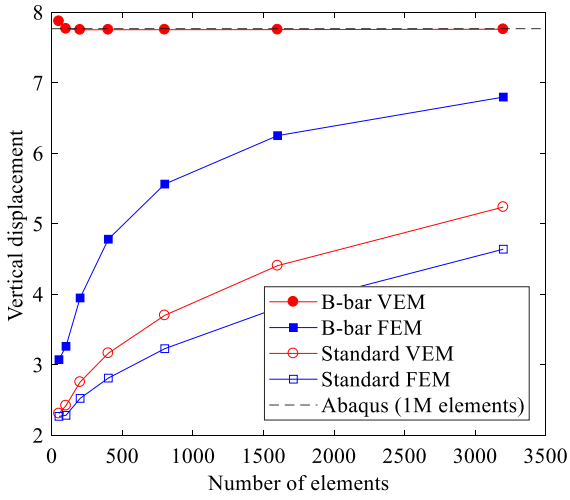

Fig. 16 Comparison between VEM and FEM for Cook's beam problem. Each point on the plots refers to a single mesh

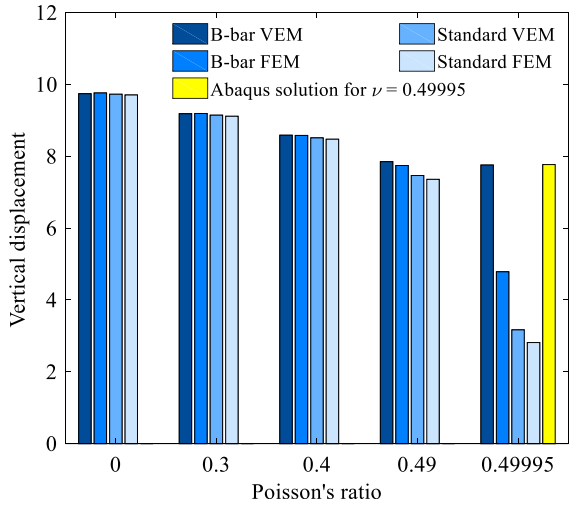

Fig. 18 Vertical displacement for Cook's beam problem according to the Poisson's ratio. For the case of $\nu = 0.49995$, the Abaqus solution uses a mesh with 1 M elements

5 Conclusion

The B-bar VEM is proposed for the analysis of both compressible and nearly incompressible materials in two- and three-dimensional problems. The material stiffness is decomposed into dilatational and deviatoric parts, and only the deviatoric part of the material stiffness is utilized for the stabilization of the element stiffness matrix. The eigenvalue analysis demonstrates that higher energy modes of VEM are clustered in certain ranges, and FEM generally provides richer eigenvalue distribution than VEM. Furthermore, the B-bar VEM captures the constant strain energy modes, while successfully eliminating higher modes associated with locking behavior for nearly incompressible materials. Four computational examples are given, i.e., cantilever, flat punch, Cook's beam benchmark, and compression of 3D constrained block. The computational results demonstrate that the optimal rate of convergence is achieved for both compressible and nearly incompressible materials regardless of element types, i.e., convex and non-convex. The B-bar method improves the accuracy of solution for both FEM and

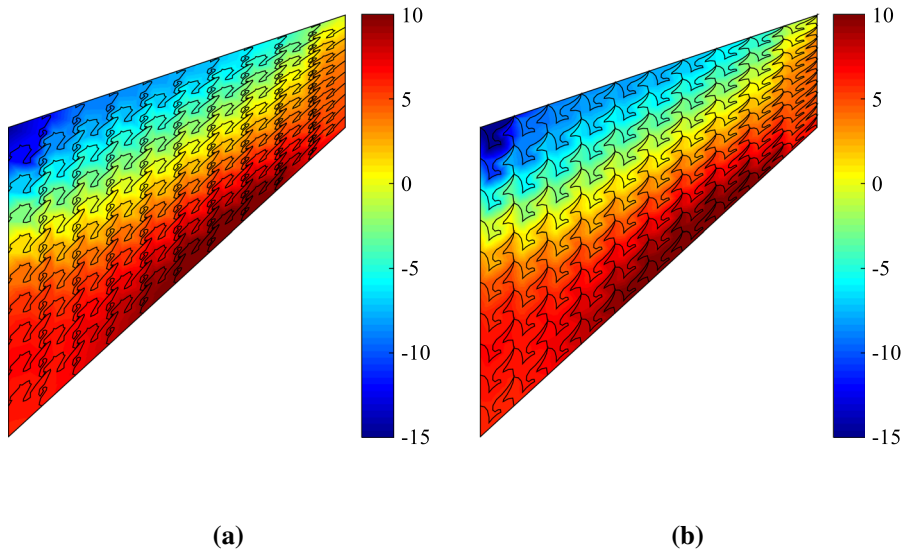

Fig. 17 Pressure filed for Cook's beam problem using **a** Pegasus mesh, and **b** Bird mesh

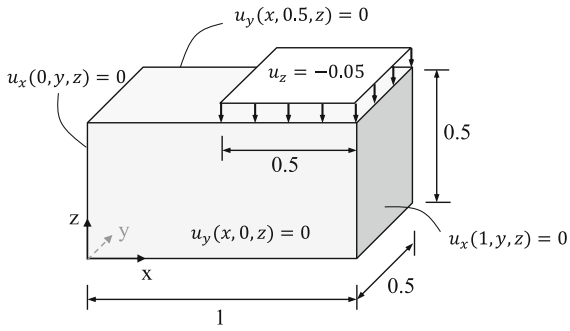

Fig. 19 Geometry and boundary conditions for the constrained block example

VEM, while the B-bar VEM provides more accurate results than the B-bar FEM. Furthermore, the B-bar VEM approach provides smooth pressure fields even with highly non-convex elements.

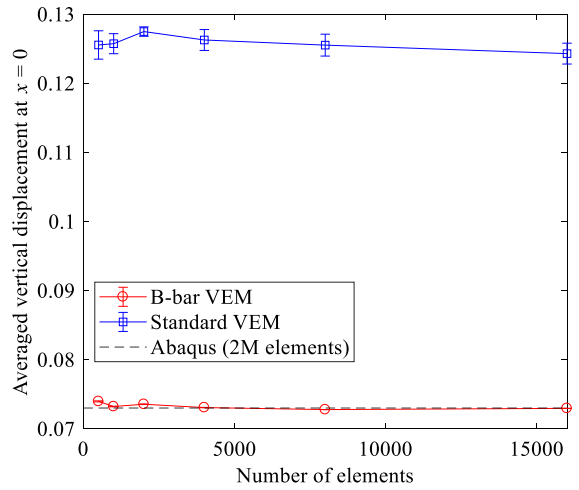

Fig. 21 Averaged displacement comparison between VEM with B-bar method and standard VEM. Each point on the plots refers to a single mesh

Fig. 20 Polyhedral mesh generation process: **a** creation of polyhedral elements within the domain, and **b** face splitting and node insertion to match the boundary conditions

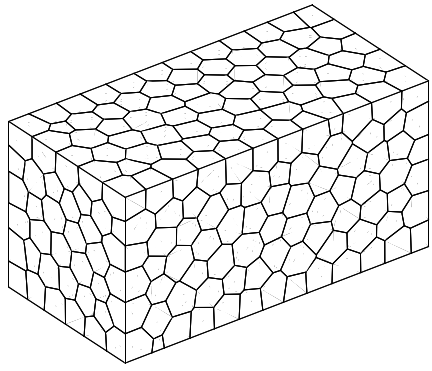

(a)

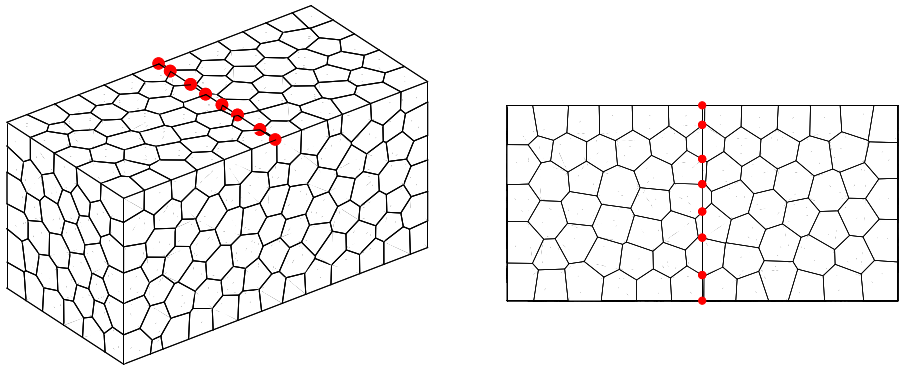

(b)

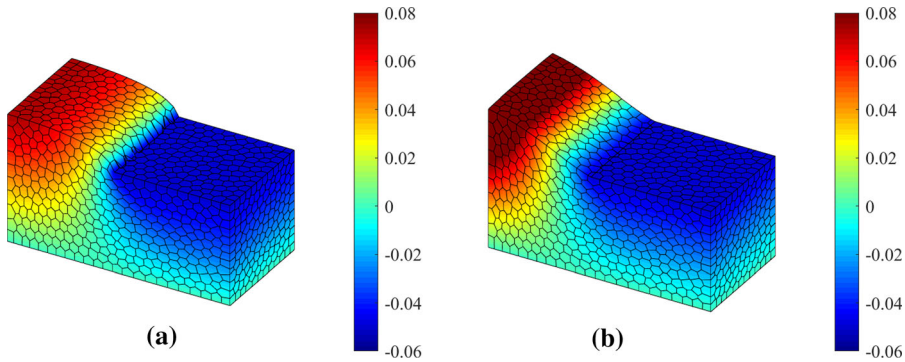

Fig. 22 Computational result of the vertical displacement using **a** B-Bar VEM, and **b** standard VEM

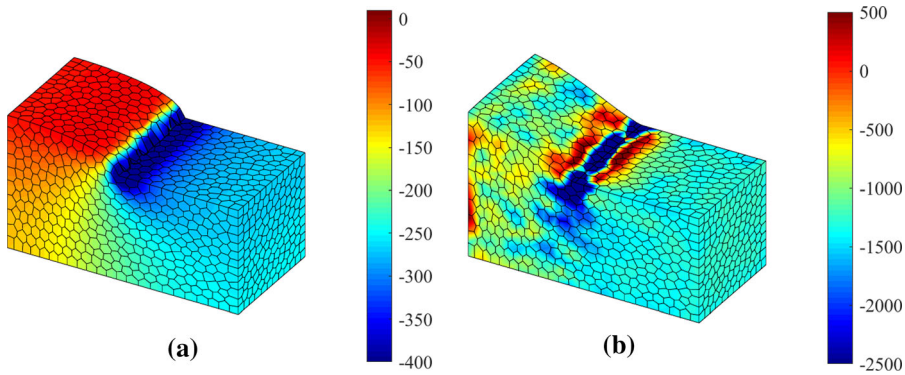

Fig. 23 Pressure filed for the constrained block problem: **a** VEM with the B-bar method, and **b** standard VEM

Acknowledgements KP acknowledges the supports from the Basic Science Research Program through the National Research Foundation of Korea (NRF) funded by the Ministry of Science, ICT & Future Planning (Grant Number: 2018R1A2B6007054), and from the Korea Institute of Energy Technology Evaluation and Planning (KETEP) funded by the Ministry of Trade, Industry & Energy (Grant Number: 20174030201480). HC and GHP acknowledge support from the US National Science Foundation (NSF) under Grant #1624232 (formerly #1437535), and the support from the Raymond Allen Jones Chair at the Georgia Institute of Technology.

Compliance with ethical standard

Conflict of interest The authors declare that they have no conflict of interests.

Appendix A. Strain decomposition

For the construction of the stability term, the material stiffness is decomposed using the spectral decomposition, as discussed in Sect. 2.4. Alternatively, the material stiffness ($\boldsymbol{C}$) can be simply decomposed on the basis of the strain components, i.e., one associated with dilatational deformation, and the other related to shear deformation. The material stiffness associated with shear deformation is given as

$$\boldsymbol{C}_\gamma = \frac{E}{2(1+\nu)} \begin{bmatrix} 0 & 0 & 0 & 0 & 0 & 0 \\ 0 & 0 & 0 & 0 & 0 & 0 \\ 0 & 0 & 0 & 0 & 0 & 0 \\ 0 & 0 & 0 & 1 & 0 & 0 \\ 0 & 0 & 0 & 0 & 1 & 0 \\ 0 & 0 & 0 & 0 & 0 & 1 \end{bmatrix} \tag{A.1}$$

and

$$\boldsymbol{C}_\gamma = \frac{E}{2(1+\nu)} \begin{bmatrix} 0 & 0 & 0 \\ 0 & 0 & 0 \\ 0 & 0 & 1 \end{bmatrix} \tag{A.2}$$

for 3D and 2D, respectively. Finally, the stability term ($\boldsymbol{K}_E^S$) can be constructed in relation with $\boldsymbol{K}_{E,dev}^C = |E|\boldsymbol{B}_c^T\boldsymbol{C}_\gamma\boldsymbol{B}_c$ and Eqs. (21)-(22). Computational results using this approach are almost identical with the results using the spectral decomposition.

Appendix B. Equivalence of B-bar formulations

We will demonstrate the connection of the proposed B-bar VEM formulation to the previous B-bar formulations introduced in [13, 16]. In particular, we will demonstrate that splitting the elasticity modulus matrix $\boldsymbol{C}$ is in fact equivalent to splitting the B matrix as is done in the classical B-bar methods in FEM [13] and the B-bar VEM formulation [16]. Again, we will use the 3D case as an example. To demonstrate the equivalence, we alternatively express $\boldsymbol{C}_{dev}$ and $\boldsymbol{C}_{dil}$ as

$$\begin{aligned}\boldsymbol{C}_{dil} &= \left(\boldsymbol{m}_1\boldsymbol{m}_1^T\right)\boldsymbol{C}\left(\boldsymbol{m}_1\boldsymbol{m}_1^T\right) \quad \text{and} \\ \boldsymbol{C}_{dev} &= \left(\boldsymbol{I}-\boldsymbol{m}_1\boldsymbol{m}_1^T\right)\boldsymbol{C}\left(\boldsymbol{I}-\boldsymbol{m}_1\boldsymbol{m}_1^T\right)\end{aligned} \tag{B.1}$$

where we call that $\boldsymbol{m}_1 = \frac{1}{\sqrt{3}}[1,1,1,0,0,0]^T$ and $\boldsymbol{I}$ is the identity matrix. Plugging the above expressions of $\boldsymbol{C}_{dev}$ and $\boldsymbol{C}_{dil}$ into the definitions of $\boldsymbol{K}_E^C$, we obtain

$$\begin{aligned}\boldsymbol{K}_E^C = &\int_E \boldsymbol{B}_c^T\left(\boldsymbol{I}-\boldsymbol{m}_1\boldsymbol{m}_1^T\right)\boldsymbol{C}\left(\boldsymbol{I}-\boldsymbol{m}_1\boldsymbol{m}_1^T\right)\boldsymbol{B}_c d\boldsymbol{x} \\ &+ \int_E \boldsymbol{B}_c^T\left(\boldsymbol{m}_1\boldsymbol{m}_1^T\right)\boldsymbol{C}\left(\boldsymbol{m}_1\boldsymbol{m}_1^T\right)\boldsymbol{B}_c d\boldsymbol{x}\end{aligned} \tag{B.2}$$

If we define

$$\begin{aligned}\boldsymbol{B}_c^{dil} &\doteq \left(\boldsymbol{m}_1\boldsymbol{m}_1^T\right)\boldsymbol{B}_c \quad \text{and} \\ \boldsymbol{B}_c^{dev} &\doteq \left(\boldsymbol{I}-\boldsymbol{m}_1\boldsymbol{m}_1^T\right)\boldsymbol{B}_c = \boldsymbol{B}_c - \boldsymbol{B}_c^{dil},\end{aligned} \tag{B.3}$$

and restrict our attention to lower-order virtual elements, we can equivalently recast the expression of $\boldsymbol{K}_{E,dev}^C$ $\boldsymbol{K}_{E,dil}^C$ and $\boldsymbol{K}_E^C$ as

$$\boldsymbol{K}_{E,dev}^C = |E|\left(\boldsymbol{B}_c^{dev}\right)^T\boldsymbol{C}\boldsymbol{B}_c^{dev}, \tag{B.4}$$

$$\boldsymbol{K}_{E,dil}^C = |E|\left(\boldsymbol{B}_c^{dil}\right)^T\boldsymbol{C}\boldsymbol{B}_c^{dil}, \tag{B.5}$$

$$\boldsymbol{K}_E^C = |E|\left(\boldsymbol{B}_c^{dev}\right)^T\boldsymbol{C}\boldsymbol{B}_c^{dev} + |E|\left(\boldsymbol{B}_c^{dil}\right)^T\boldsymbol{C}\boldsymbol{B}_c^{dil}. \tag{B.6}$$

In addition, because $\left(\boldsymbol{I}-\boldsymbol{m}_1\boldsymbol{m}_1^T\right)\boldsymbol{C}\boldsymbol{m}_1\boldsymbol{m}_1^T = 0$, we recover

$$\begin{aligned}\boldsymbol{K}_E^C &= |E|\left(\boldsymbol{B}_c^{dev}+\boldsymbol{B}_c^{dil}\right)^T\boldsymbol{C}\left(\boldsymbol{B}_c^{dev}+\boldsymbol{B}_c^{dil}\right) \\ &= |E|(\boldsymbol{B}_c)^T\boldsymbol{C}(\boldsymbol{B}_c),\end{aligned} \tag{B.7}$$

which is the same as the construction in reference [16].

Now let us look at the matrix $\boldsymbol{B}_c^{dil}$. Because

$$\left(\boldsymbol{m}_1\boldsymbol{m}_1^T\right)\boldsymbol{b}\left(\Pi^0\phi_i\right) = \frac{1}{3}\begin{bmatrix} \frac{\partial\Pi^0\phi_i}{\partial x} & \frac{\partial\Pi^0\phi_i}{\partial y} & \frac{\partial\Pi^0\phi_i}{\partial z} \\ \frac{\partial\Pi^0\phi_i}{\partial x} & \frac{\partial\Pi^0\phi_i}{\partial y} & \frac{\partial\Pi^0\phi_i}{\partial z} \\ \frac{\partial\Pi^0\phi_i}{\partial x} & \frac{\partial\Pi^0\phi_i}{\partial y} & \frac{\partial\Pi^0\phi_i}{\partial z} \\ 0 & 0 & 0 \\ 0 & 0 & 0 \\ 0 & 0 & 00 \end{bmatrix}, \tag{B.8}$$

the matrix form of $\boldsymbol{B}_c^{dil} \doteq \left(\boldsymbol{m}_1\boldsymbol{m}_1^T\right)\boldsymbol{B}_c$ is the same as the $\bar{\boldsymbol{B}}^{dil} = 1/|E|\int_E \boldsymbol{B}^{dil}\mathrm{d}\boldsymbol{x}$ in the classical B-bar method in FEM [13] and the one in the B-bar VEM formulation in [16].

Based on the above analysis, we conclude that the proposed B-bar VEM formulation and the B-bar VEM formulation in [16], although they start from different perspectives, will lead to the same consistency part of the stiffness matrix. The main difference between the two formulations lies in how we construct the stability part of the stiffness matrix. In addition, we also note that the present B-bar VEM formulation enjoys more generality and can be more straightforwardly applied to higher-order cases and anisotropies solids.

Appendix C. Equivalence between B-bar VEM and mixed (displacement–pressure) VEM formulations

In this appendix, we will demonstrate that the proposed B-bar VEM formulation is equivalent to the two-field mixed VEM formulation [26], which is another popular approach to model nearly incompressible solids. We note that such equivalence is also explored in the FEM setting [27].

Based on the decomposition of the elastic modulus matrix $\boldsymbol{C}$ into the deviatoric and dilatational components [i.e., Equation (12)], we can express the stress–strain relationship as

$$\begin{aligned}\boldsymbol{\sigma}(\boldsymbol{u}) &= \boldsymbol{C}_{dev}\boldsymbol{\varepsilon}(\boldsymbol{u}) + \boldsymbol{C}_{dil}\boldsymbol{\varepsilon}(\boldsymbol{u}) \\ &= \boldsymbol{C}_{dev}\boldsymbol{\varepsilon}(\boldsymbol{u}) + \lambda_1\boldsymbol{m}_1\boldsymbol{m}_1^T\boldsymbol{\varepsilon}(\boldsymbol{u}).\end{aligned} \tag{C.1}$$

If we introduce a pressure field given by $p = \lambda_1\boldsymbol{m}_1^T\boldsymbol{\varepsilon}(\boldsymbol{u})$, where we recall that $\boldsymbol{m}_1 = \frac{1}{\sqrt{2}}[1,1,0]^T$ in 2D and $\boldsymbol{m}_1 = \frac{1}{\sqrt{3}}[1,1,1,0,0,0]^T$ in 3D

and λ_1 is the eigenvalue of $\boldsymbol{C}$ associated with $\boldsymbol{m}_1$, the stress–strain relationship is expressed as

$$\boldsymbol{\sigma}(\boldsymbol{u},p) = \boldsymbol{C}_{\boldsymbol{dev}}\boldsymbol{\varepsilon}(\boldsymbol{u}) + p\boldsymbol{m}_1 \quad \text{with } p = \lambda_1 \boldsymbol{m}_1^T \boldsymbol{\varepsilon}(\boldsymbol{u}) \tag{C.2}$$

To derive a two-field mixed VEM approximation, we introduce a discrete pressure space $\mathcal{Q}_h$ as

$$\mathcal{Q}_h = \left\{ p_h \in L^2(\Omega_h) : p_h|_E \in \mathcal{P}_0(E), \forall E \in \Omega_h \right\} \tag{C.3}$$

which contains element-wise constant pressure field. According to Eq. (C.2), the pressure field within element E is given by

$$\begin{aligned} p_h|_E &= \frac{1}{|E|}\int_E \lambda_1 \boldsymbol{m}_1^T \boldsymbol{\varepsilon}(\boldsymbol{u}_h) d\boldsymbol{x} = \lambda_1 \boldsymbol{m}_1^T \boldsymbol{\varepsilon}\left(\boldsymbol{\Pi}^0 \boldsymbol{u}_h\right) \\ &= \lambda_1 \boldsymbol{m}_1^T \boldsymbol{B}_c \boldsymbol{u}_E \end{aligned} \tag{C.4}$$

where $\boldsymbol{u}_E$ is the nodal displacement vector of element E. This gives the relation

$$\boldsymbol{m}_1^T \boldsymbol{B}_c \boldsymbol{u}_E - \frac{1}{\lambda_1} p_h|_E = 0 \tag{C.5}$$

In addition, plugging Eq. (14) into Eq. (C.4), we obtain the following relation:

$$\begin{aligned} \boldsymbol{K}_E \boldsymbol{u}_E &= \left(\boldsymbol{K}_{E,dev}^C + \boldsymbol{K}_E^S + \boldsymbol{K}_{E,dil}^C \right) \boldsymbol{u}_E \\ &= \left(\boldsymbol{K}_{E,dev}^C + \boldsymbol{K}_E^S \right) \boldsymbol{u}_E + \lambda_1 |E| \boldsymbol{B}_c^T \boldsymbol{m}_1 \boldsymbol{m}_1^T \boldsymbol{B}_c \boldsymbol{u}_E \\ &= \left(\boldsymbol{K}_{E,dev}^C + \boldsymbol{K}_E^S \right) \boldsymbol{u}_E + |E| \boldsymbol{B}_c^T \boldsymbol{m}_1 p_h|_E \end{aligned} \tag{C.6}$$

Combining Eqs. (C.5) and (C.6), we arrive at the following element-level stiffness matrix

$$\boldsymbol{K}_E^{\boldsymbol{u},p} = \begin{bmatrix} \boldsymbol{K}_{E,dev}^C + \boldsymbol{K}_E^S & |E| \boldsymbol{B}_c^T \boldsymbol{m}_1 \\ |E| \boldsymbol{m}_1^T \boldsymbol{B}_c & \dfrac{1}{\lambda_1} \end{bmatrix} \tag{C.7}$$

which is the local stiffness matrix for the standard two-field mixed VEM approximation. In summary, the above analysis demonstrates that the proposed B-bar VEM formulation is equivalent to the two-field mixed VEM approximation for all λ_1 values except for $\lambda_1 = \infty$, meaning that the two formulations will deliver identical results. The advantage of the proposed B-bar VEM formulation over the mixed VEM formulation is that the B-bar VEM formulation has fewer degrees of freedom. When λ_1 is infinity, meaning the solid is purely incompressible, the B-bar VEM formulation is not well-defined but the two-field mixed formulation still applies.

References

1. Masud A, Xia K (2005) A stabilized mixed finite element method for nearly incompressible elasticity. J Appl Mech 72(5):711
2. Ortiz-Bernardin A, Hale JS, Cyron CJ (2015) Volume-averaged nodal projection method for nearly-incompressible elasticity using meshfree and bubble basis functions. Comput Methods Appl Mech Eng 285:427–451
3. Scovazzi G, Carnes B, Zeng X, Rossi S (2016) A simple, stable, and accurate linear tetrahedral finite element for transient, nearly, and fully incompressible solid dynamics: a dynamic variational multiscale approach. Int J Numer Meth Eng 106:799–839
4. Boffi D, Brezzi F, Fortin M (2013) Mixed finite element methods and applications. Springer, Berlin
5. Beirão da Veiga L, Brezzi F, Dassi F, Marini LD, Russo A (2018) Lowest order Virtual Element approximation of magnetostatic problems. Comput Methods Appl Mech Eng 332:343–362
6. Chi H, Pereira A, Menezes IFM, Paulino GH (2019) Virtual element method (VEM)-based topology optimization: an integrated framework. *Structural and Multidisciplinary Optimization*, p. under review
7. Mengolini M, Benedetto MF, Aragón AM (2019) An engineering perspective to the virtual element method and its interplay with the standard finite element method. Comput Methods Appl Mech Eng 350:995–1023
8. Park K, Chi H, Paulino GH (2019) On nonconvex meshes for elastodynamics using virtual element methods with explicit time integration. Comput Methods Appl Mech Eng 356:669–684
9. Ahmad B, Alsaedi A, Brezzi F, Marini LD, Russo A (2013) Equivalent projectors for virtual element methods. Comput Math Appl 66(3):376–391
10. Beirão da Veiga L, Dassi F, Russo A (2017) High-order Virtual Element Method on polyhedral meshes. Comput Math Appl 74(5):1110–1122
11. Beirão da Veiga L, Brezzi F, Marini LD, Russo A (2014) The hitchhiker's guide to the virtual element method. Math Models Methods Appl Sci 24(8):1541–1573
12. Oberrecht SP, Novák J, Krysl P (2014) B-bar FEMs for anisotropic elasticity. Int J Numer Meth Eng 98:92–104
13. Hughes TJR (1980) Generalization of selective integration procedures to anisotropic and nonlinear media. Int J Numer Methods Eng, 1413–1418
14. Dassi F, Mascotto L (2018) Exploring high-order three dimensional virtual elements: bases and stabilizations. Comput Math Appl 75(9):3379–3401
15. Beirão da Veiga L, Dassi F, Russo A (2020) A C1 Virtual Element Method on polyhedral meshes. Computers and Mathematics with Applications, vol. In press

16. Park K, Chi H, Paulino GH (2020) Numerical recipes for elastodynamic virtual element methods with explicit time integration. Int J Numer Meth Eng 121:1–31
17. Beirão da Veiga L, Brezzi F, Marini LD (2013) Virtual elements for linear elasticity problems. SIAM J Numer Anal 51(2):794–812
18. Gain AL, Talischi C, Paulino GH (2014) On the Virtual Element Method for three-dimensional linear elasticity problems on arbitrary polyhedral meshes. Comput Methods Appl Mech Eng 282:132–160
19. Reddy BD, van Huyssteen D (2019) A virtual element method for transversely isotropic elasticity. Comput Mech 64(4):971–988
20. Wriggers P, Hudobivnik B, Korelc J (2018) Efficient low order virtual elements for anisotropic materials at finite strains. In: Oñate E, Peric D, de Souza Neto E, Chiumenti M (eds) Advances in Computational Plasticity. Springer, Berlin, pp 417–434
21. Wriggers P, Reddy BD, Rust W, Hudobivnik B (2017) Efficient virtual element formulations for compressible and incompressible finite deformations. Comput Mech 60(2):253–268
22. Wachspress EL (1975) A rational finite element basis. Academic Press, New York
23. Timoshenko SP, Goodier JN (1970) Theory of elasticity, 3rd edn. McGraw-Hill, New York
24. Choi H, Park K (2019) Removing mesh bias in mixed-mode cohesive fracture simulation with stress recovery and domain integral. Int J Numer Meth Eng 120:1047–1070
25. Abaqus, *Abaqus 3D Experience R2016X*. Dassault Systemes SIMULIA, 2016
26. Chi H, da Veiga LB, Paulino GH (2017) Some basic formulations of the virtual element method (VEM) for finite deformations. Comput Methods Appl Mech Eng 318:148–192
27. Malkus DS, Hughes TJR (1978) Mixed finite element methods—reduced and selective integration techniques: a unification of concepts. Comput Methods Appl Mech Eng 15(1):63–81